Using Plasmonic Copper Sulfide Nanocrystals as Smart Light-Driven Sterilants

Zhen Liu,[†] Xianjun Liu,[‡] Yingda Du,[§] Jinsong Ren,[*,†] and Xiaogang Qu[*,†]

[†]State Key Laboratory of Rare Earth Resource Utilization and Laboratory of Chemical Biology, Changchun Institute of Applied Chemistry, Changchun 130022, China, [‡]Bethune Institute of Epigenetic Medicine, First Hospital of Jilin University, Changchun 130021, China, and [§]College of Life Science, Jilin University, Changchun, Jilin 130012, China

ABSTRACT As an efficient route to control pet overpopulation and develop neutered experimental animals, male sterilization *via* surgical techniques, chemical injections, and antifertility vaccines has brought particular attention recently. However, these traditional ways usually induce long-term adverse reactions, immune suppression, and serious infection and pain. To overcome the above limitations, we developed a platform in the present study by using plasmonic copper sulfide nanocrystals ($Cu_{2-x}S$ NCs) as intelligent light-driven sterilants with ideal outcomes. Upon NIR laser irradiation, these well-prepared $Cu_{2-x}S$ NCs can possess NIR-induced hyperthermia and generate high levels of reactive oxygen species (ROS). Due to the cooperation of photothermal and photodynamic effects, these nanocrystals exhibited NIR-mediated toxicity toward Sertoli cells both *in vitro* and *in vivo* in a mild manner. We attribute the potential mechanism of cellular injury to the apoptosis-related death and denaturation of protein in the testicles. Furthermore, the possible metabolism route and long-term toxicity of these nanocrystals after testicular injection indicate their high biocompatibility. Taking together, our study on the NIR-induced toxicity of $Cu_{2-x}S$ NCs provides keen insights for the usage of plasmonic nanomaterials in biomedicine.
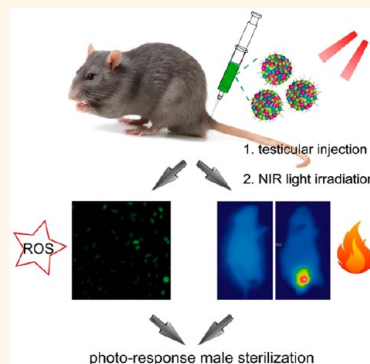
KEYWORDS: copper sulfide · photothermal effect · photodynamic effect · male sterilization · fertility

With the rapid development of modern society, permanent male sterilization has been considered as the most efficient approach to achieve neutered experimental animals and control the exploding population of household pets.[1−3] Current methods of using surgical techniques, chemical injection, and antifertility vaccines have addressed the crucial aspect of male sterilization with significant outcomes. Despite their usefulness, surgical sterilization in males, namely, orchidectomy or castration, usually comprises multistep manipulations, which are directly dependent on the skill proficiency of veterinarians.[4,5] Other routes such as chemical injection and antifertility vaccines can induce long-term adverse reactions and unwanted immune suppression, as well as undergo recurrence of fertility over chemical or immune periods.[6,7] In this regard, a nonsurgical yet efficient alternative to permanent male sterilization with negligible side effects is highly desirable.

Due to their versatile functionality and unique physical properties, nanostructures have been explored as emerging theranostic platforms for disease diagnosis and therapy.[8−10] Among all these studies, plasmonic materials such as noble metal nanostructures, carbon nanotubes, graphene, and organic polymers can absorb energy from photons and dissipate it in the form of heat and energy totally or partially.[11−14] These materials with ideal near-infrared (NIR) absorbance can act as photoinduced agents in photoacoustic (PA) imaging and photothermal therapy (PTT) of solid tumor.[15−18] Regardless of recent studies on plasmonic materials that have made huge progress in cancer detection and treatment, the new utility of these materials in other biomedicine fields is still in its infancy. Owing to the serious injury in spermatogenesis and destruction of testicular function, hyperthermia can lead to temporary or permanent male infertility. In that case, we envision that male sterilization may be well

mediated *via* the photothermal effect of these plasmonic nanomaterials. However, several obstacles badly restrict their practical usage in reproductive medicine. For example, gold-based nanostructures always lose their stable NIR absorbance after laser irradiation.[19,20] High cost and low abundance of noble metals limit their commercial translation from the lab to the clinic.[21,22] Nonbiodegradable carbon nanotubes and graphene may remain in the body for a long time after injection.[23−25] More significantly, hyperthermia around the testicles can cause grievous testicular irritation, which brings immoderate pain to animals and excess risk to veterinarians. Accordingly, it is still a major challenge to explore a highly efficient nanosized sterilant for male sterilization with a mild manner.

Arising from their strong localized surface plasmon resonance (LSPR) from the red edge to the NIR region of light, a series of plasmonic copper chalcogenide-based nanomaterials have been employed as PA and PTT agents recently.[26−44] These materials are composed of low-cost elements and are easy to synthesize with a large-scale route. Moreover, it is well known that Cu(I) species in biological media can produce reactive oxygen species (ROS) *via* a similar Haber−Weiss cycle. Cu(II) ions can be reduced to Cu(I) species by intracellular glutathione or ascorbic acid.[45−47] These unstable but highly active ROS including hydroxyl radicals ($\cdot$OH), singlet oxygen ($^1O_2$), and peroxides (R−O−O$\cdot$) could irreversibly induce serious damage toward targeted organs and tissues. Encouraged by this evidence, we demonstrate that plasmonic copper sulfide nanocrystals ($Cu_{2−x}S$ NCs) can act as smart light-driven sterilants for permanent male sterilization. To the best of our knowledge, it is the first example showing that metal chalcogenide-based materials can be used as theranostic agents in reproductive medicine. In our present design, these nanocrystals can possess a mild hyperthermia and sensitize the formation of ROS with the assistance of 980 nm irradiation, resulting in further irreversible male sterilization. Attractively, $Cu_{2−x}S$ NCs induce generation of ROS only upon irradiation with NIR light, whereas no ROS can be detected in the group of $Cu_{2−x}S$ NCs without irradiation and in the irradiation group without nanocrystals. We attribute the potential mechanism of gonad injury to apoptosis-induced death and excess expression of caspase proteins in Sertoli cells. The coordination of photothermal and photodynamic effects of $Cu_{2−x}S$ NCs upon NIR irradiation not only allows a tolerable temperature around the testicles but also affords a mild platform for permanent male sterilization. Thus, our present strategy identifies a new usage of $Cu_{2−x}S$ NCs and provides a simple but powerful system in the field of reproductive medicine.

RESULTS AND DISCUSSION

The rational synthesis of plasmonic $Cu_{2−x}S$ NCs and their further usage in male sterilization are illustrated in Figure 1A. Hydrophobic nanocrystals coated with oleylamine (OM) were first prepared *via* a modified thermal decomposition method.[48] Second, a ligand exchange procedure was used to alter the surface property. In detail, OM coated on the surface of hydrophobic nanocrystals was exchanged by 6-aminocaproic acid (6-ACA) to result in hydrophilic nanocrystals. Figure 1B shows photos of as-prepared nanocrystals dispersed into different solvents before and after the ligand modification. As expected, hydrophobic nanocrystals were well dispersed in nonpolar chloroform ($CHCl_3$), while hydrophilic NCs exhibited a high solubility in water. TEM images indicated that there were no obvious differences in size and shape between hydrophobic and hydrophilic NCs (Figure 1C and D). HR-TEM images indicated both nanocrystals with sizes ranging from 12 to 20 nm. Diffraction peaks observed in wide-angle XRD patterns of both samples matched well with the crystal phase of chalcocite (JCPDS no. 02-1294), although minor djurleite phase could also be detected (Figure 1E and Figure S1A). The selective area electronic diffraction (SAED) pattern of hydrophilic NCs additionally proved their high crystallinity. Energy-dispersive spectroscopy (EDS) analysis demonstrated the presence of Cu, S, C, O, and N in both samples (Figure 1F and Figure S1B). The detailed chemical composition of hydrophilic nanorcystals was evaluated by ICP-MS, which could be calculated to be $Cu_{1.9}S$. Then, FT-IR spectra were used to identify the efficiency of ligand exchange (Figures S1C and S1D). Both nanorcystals exhibited similar spectra in the N−H/O−H stretching vibration, symmetric/asymmetric stretching vibrations of methylene, N−H bending mode, and C−N stretching mode. However, the peak of the C≡C−H stretching vibration at 3007 $cm^{−1}$ partly disappeared in the spectrum of the hydrophilic NCs, suggesting the replacement of OM by 6-ACA.[49] The zeta-potential of hydrophilic nanocrystals in 0.9% NaCl solution was about +9.6 mV and got close to the neutral points. The above results showed that the hydrophobic NCs were successfully changed to hydrophilic nanocrystals by our ligand exchange strategy. More importantly, it is worth noting that no changes occurred in the morphological character and crystal phase before and after modification.

UV−vis−NIR spectra demonstrated that $Cu_{2−x}S$ NCs in water exhibited a broad absorption in the NIR region ranging from 700 to 1100 nm, favoring their light-induced properties (Figure 2A and Figure S2C). As illustrated in Figures S2A and S2B, pure water exhibited a slight absorption around 1000 nm, whereas our sample still held a strong absorption in the NIR region after baseline deduction. To evaluate the photothermal properties of $Cu_{2−x}S$ NCs upon NIR irradiation, temperature changes of the suspension under different treatments were recorded. As depicted in Figure 2B and C, the temperatures of $Cu_{2−x}S$ NCs samples increased rapidly along with the increase of the irradiation
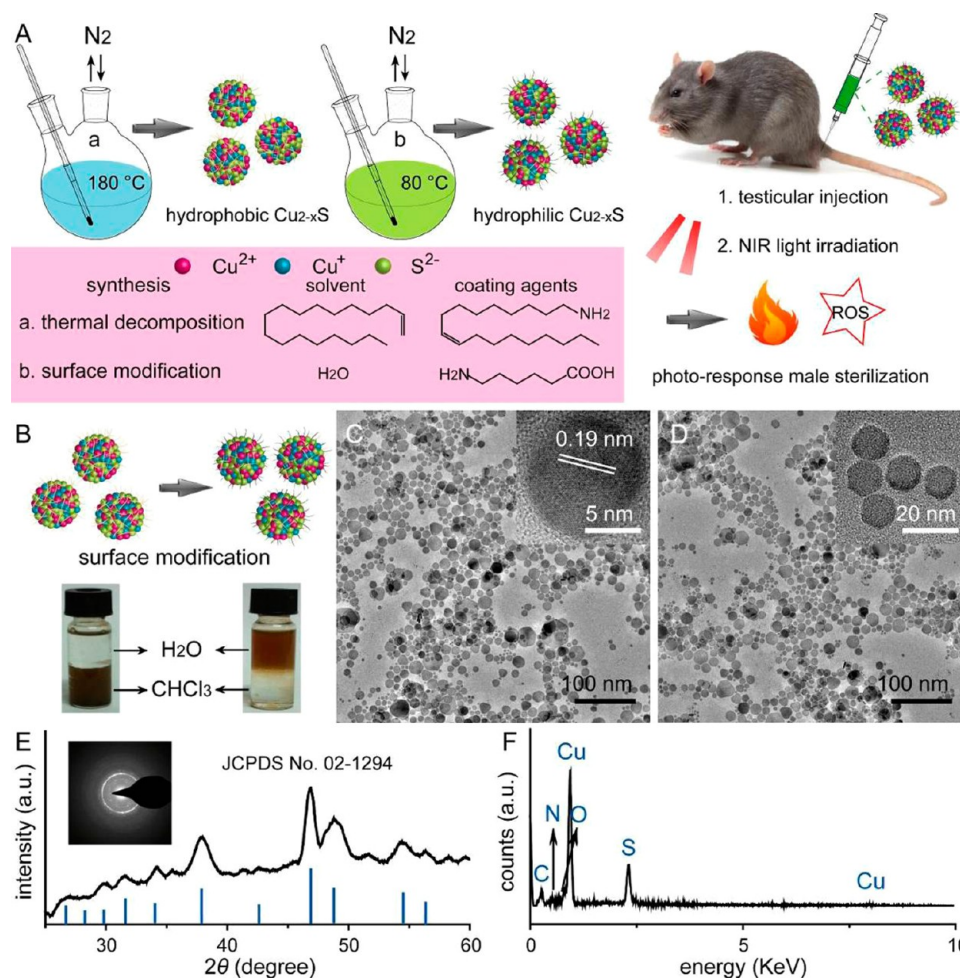
Figure 1. Schematic illustration of the two-step synthesis and biorelated usage of hydrophilic $Cu_{2-x}S$ nanocrystals (A). Photo of $Cu_{2-x}S$ NCs dispersed in different solvents (H_2O and $CHCl_3$) before and after ligand exchange (B). TEM images of hydrophobic $Cu_{2-x}S$ NCs (C) and hydrophilic $Cu_{2-x}S$ NCs (D). HR-TEM images of hydrophobic $Cu_{2-x}S$ NCs and hydrophilic $Cu_{2-x}S$ NCs (insets of C and D). Wide-angle XRD pattern (E) and EDS spectra (F) of hydrophilic $Cu_{2-x}S$ NCs. SAED image of hydrophilic $Cu_{2-x}S$ NCs (inset of E).

period and sample concentrations. In detail, the temperature change of $Cu_{2-x}S$ NCs (0.2 mg/mL) could easily reach 15 °C within 5 min after 980 nm laser irradiation (1.5 W/cm^2), while the 0.9% NaCl solution exhibited a mild temperature change within 5 °C under the same conditions. On the basis of the heating—cooling result, the photothermal conversion efficiency of $Cu_{2-x}S$ NCs could be calculated to be 15%, which was similar to some previous studies (Figure S2D).[50,51] The above results implied that $Cu_{2-x}S$ NCs could rapidly and efficiently convert light energy into heat and remain at the local temperature for a period of time. As is well known, Cu(II) ions can be reduced to Cu(I) ions by an intracellular reducing agent and Cu(I) ions in biological media can produce ROS. Illumined by these facts, we rationally evaluated the light-induced ROS generation of these $Cu_{2-x}S$ NCs. In our present design, ROS production was confirmed *via* the fluorescence quantity of dichlorofluorescein diacetate (DCFH-DA), which could be oxidized by ROS to fluorescent 2,7-dichlorofluorescein (DCF).[52,53] As a broad-spectrum oxidation-sensitive

reagent, DCFH-DA was applied to determine the total generation of various ROS, such as $\cdot$OH, $^1O_2$, and R—O—O$\cdot$. Measured *via* a Kodak imaging system, ROS generation occurred only in the presence of $Cu_{2-x}S$ NCs and NIR irradiation, whereas no ROS could be detected in $Cu_{2-x}S$ NC groups and NIR irradiation groups (Figure 2E). Compared with standard ROS-induced agents such as H_2O_2 and NaClO, $Cu_{2-x}S$ NCs with similar concentrations could introduce equivalent ROS after NIR irradiation, indicating their significant photodynamic effect. Then, we tested the thermal stability and photostability of these nanocrystals. Hydrophilic $Cu_{2-x}S$ NCs were found to be colloidal without any precipitation even up to 50 °C in a 0.9% NaCl solution (Figure 2D). Moreover, there were no differences in UV—vis—NIR absorption, morphology, and size before and after a long-term NIR irradiation (Figure S2E and F). These results imply the unexceptionable photostability of $Cu_{2-x}S$ NCs and their negligible loss in NIR absorbance after high-power NIR laser irradiation.

Prior to using $Cu_{2-x}S$ NCs for biomedical applications, it was essential to evaluate their degradability,
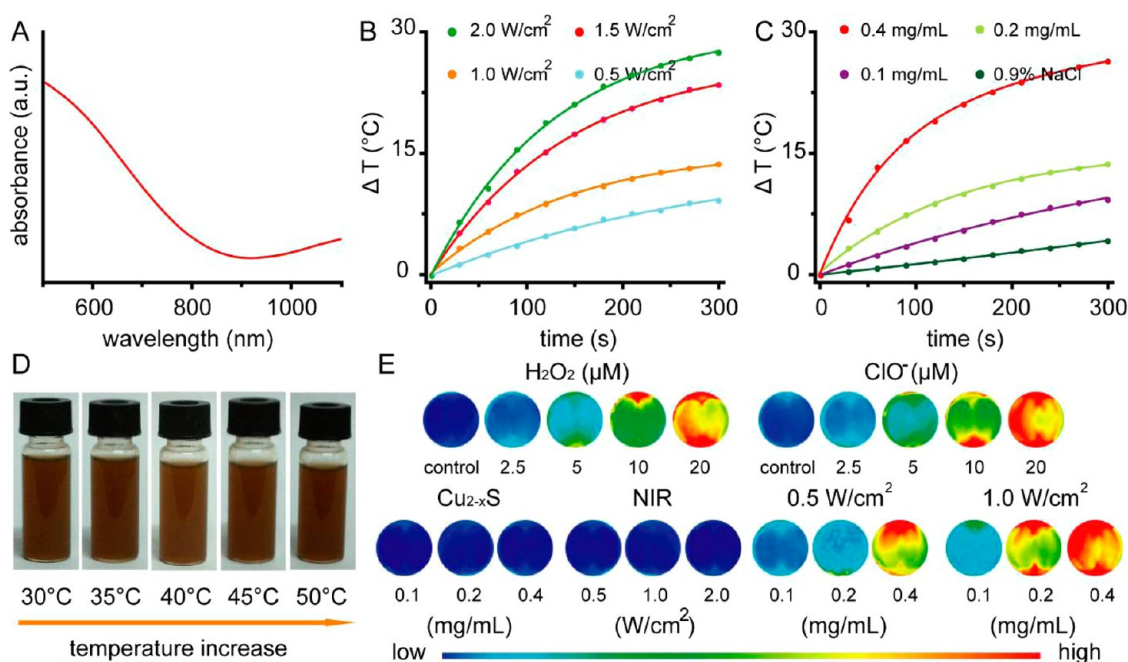
Figure 2. UV−vis−NIR absorption spectra of $Cu_{2-x}S$ NCs in water (A). Temperature change of $Cu_{2-x}S$ NCs (0.2 mg/mL) irradiated by a 980 nm laser with different power intensities (B). Temperature change of $Cu_{2-x}S$ NCs with different concentrations irradiated by a 980 nm laser with a power intensity of 1.5 W/cm² (C). Photos of $Cu_{2-x}S$ NCs in a 0.9% NaCl solution (1 mg/mL) incubated at various temperatures for 10 min (D). Fluorescence imaging of ROS generation detected by DCFH-DA assay (E). Upper line: Standard H_2O_2 and NaClO solutions with different concentrations treated with DCFH-DA. Lower line: Our experimental samples under various conditions treated with DCFH-DA.

cytotoxicity, and blood compatibility. $Cu_{2-x}S$ NCs (0.2 mg/mL) were incubated in PBS buffer with different pH values (pH 7.4 and pH 4.5). One week after incubation, it was hard to detect Cu ions in the group of pH 7.4, whereas a minor amount of Cu ions could be found in the group of pH 4.5 *via* the ICP-MS method. The above results could be attributed to the interaction between H^+ ions and $Cu_{2-x}S$ NCs. In detail, Cu(I) species could transform into other modalities upon different reaction conditions. More importantly, H^+ ions could catalyze the disproportionation reaction of Cu(I) species, which thus caused the dissolution of these nanocrystals. However, owing to the successful and efficient coating of 6-ACA on the surface, these nanocrystals could not rapidly dissolve in the buffer system. MTT assay and live/dead staining indicated that the cellular viability and morphology were not affected by $Cu_{2-x}S$ NCs under the present experimental concentrations, verifying that $Cu_{2-x}S$ NCs possess extremely low cytotoxicity (Figure S3). In addition, an *in vitro* hemolytic assay was used to define the interaction between $Cu_{2-x}S$ NCs and various blood components. Nearly no hemolysis of red blood cells could be found even with the maximal incubation concentration (Figure S4 and Table S1).[54,55] These results demonstrated the negligible *in vitro* toxicity and excellent blood compatibility of $Cu_{2-x}S$ NCs, as well as their feasibility for further biorelated usages.

To verify the light-induced cytotoxicity of $Cu_{2-x}S$ NCs, Sertoli cells were first incubated with our nanocrystals

and then irradiated with a 980 nm laser. As shown in Figure 3A, $Cu_{2-x}S$ NCs exhibited an enhanced light-induced cytotoxicity with the increase of nanocrystal concentrations and NIR laser irradiation periods. The light-induced IC_{50} value of $Cu_{2-x}S$ NCs was lower than 0.032 mg/mL under a 3 min irradiation (1.0 W/cm²). By increasing the irradiation period to 6 min, the IC_{50} value decreased to 0.015 mg/mL. In contrast, individually the 980 nm laser and the $Cu_{2-x}S$ NCs exhibited no significant cytotoxicity upon similar treatments. Live/dead staining and typan blue staining further provided visible data to reconfirm our results that $Cu_{2-x}S$ NCs possess a light-induced cytotoxicity against Sertoli cells (Figure 3B and C). Besides the photothermal effect of $Cu_{2-x}S$ NCs upon NIR irradiation, it was noteworthy that cellular death could also be caused by the light-induced generation of ROS in Sertoli cells, which prompted us to examine the *in vitro* photodynamic effect of $Cu_{2-x}S$ NCs (Figure 2E). To obtain more precise evidence, we assessed intracellular ROS levels by using fluorescence microscopy and a flow cytometry assay. Green fluorescence with higher intensity could be detected in the $Cu_{2-x}S$+NIR group (Figure 3D). Mean the fluorescence intensity of DCF in the $Cu_{2-x}S$+NIR group was nearly three times those of other groups, indicating that Sertoli cells internalized with $Cu_{2-x}S$ NCs had higher amounts of ROS upon 980 nm irradiation (Figure S5).

After understanding the light-driven destruction capabilities of $Cu_{2-x}S$ NCs toward Sertoli cells, it was
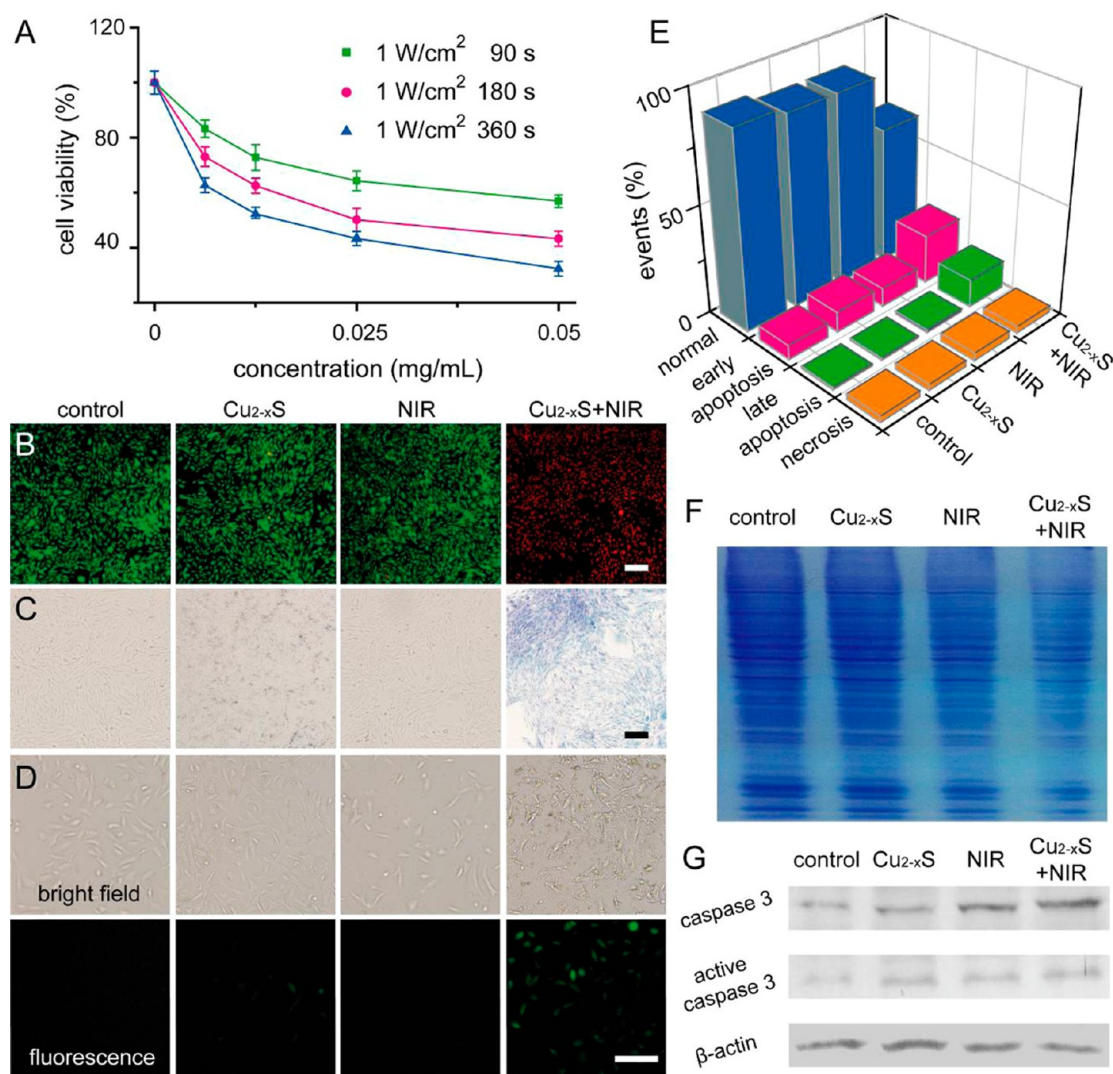
Figure 3. Viabilities of Sertoli cells incubated with Cu$_{2-x}$S NCs of different concentrations under various conditions (A). Fluorescence images of calcein AM/PI-stained cells (B), optical images of trypan blue-stained cells (C), and levels of the ROS generation based on fluorescence images (D) after different treatments. The scale bar equals 100 μm. Apoptosis/necrosis analysis based on flow cytometry results (E), total-protein analysis *via* Coomassie brilliant blue staining (F), and Western blotting analysis of apoptosis-associated protein (G).

essential to differentiate the contribution of photodynamic NCs from that of photothermal ones. To avoid the intracellular damage caused by ROS, dimethyl sulfoxide (DMSO) and uric acid (UA) were selected as efficient ROS scavengers.[56,57] As shown in Figure S6A, no obvious green fluorescence from DCF could be detected in the Cu$_{2-x}$S+NIR+UA/DMSO group, indicating that the cooperation of UA and DMSO efficiently inhibited the generation of ROS. Based on our MTT assays, there was more cellular death in the Cu$_{2-x}$S+NIR groups compared to the Cu$_{2-x}$S+NIR+UA/DMSO groups upon different incubation concentrations (Figure S6B). In detail, there was 46% cellular death caused by the photothermal effect of Cu$_{2-x}$S after NIR irradiation (0.05 mg/mL, 1 W/cm^2, 6 min), whereas the photodynamic effect induced 22% cellular death. Quantitatively, the amount of cellular death caused by the photothermal effect was nearly 2 times that induced

via the photodynamic effect. Moreover, the present ROS scavengers could not lead to the death of Sertoli cells, further suggesting the potential of our experimental design and hypothesis.

We then explored the possible mechanism of cellular death cased by Cu$_{2-x}$S NCs upon NIR irradiation. Flow cytometry results demonstrated that more apoptosis and necrosis occurred in the Cu$_{2-x}$S+NIR group, thereby revealing that Cu$_{2-x}$S NCs were able to trigger severe light-induced cytotoxicity due to their dual light-driven effects (Figure 3E and Figure S7). Nearly 40% of Sertoli cells in the Cu$_{2-x}$S+NIR group underwent early apoptosis, late apoptosis, and necrosis. However, only a small amount of apoptosis and necrosis occurred in the other three groups (less than 15%), revealing that both Cu$_{2-x}$S NCs and NIR light could induce serious cellular damage. Recent studies showed that hyperthermia and a high level of ROS could lead
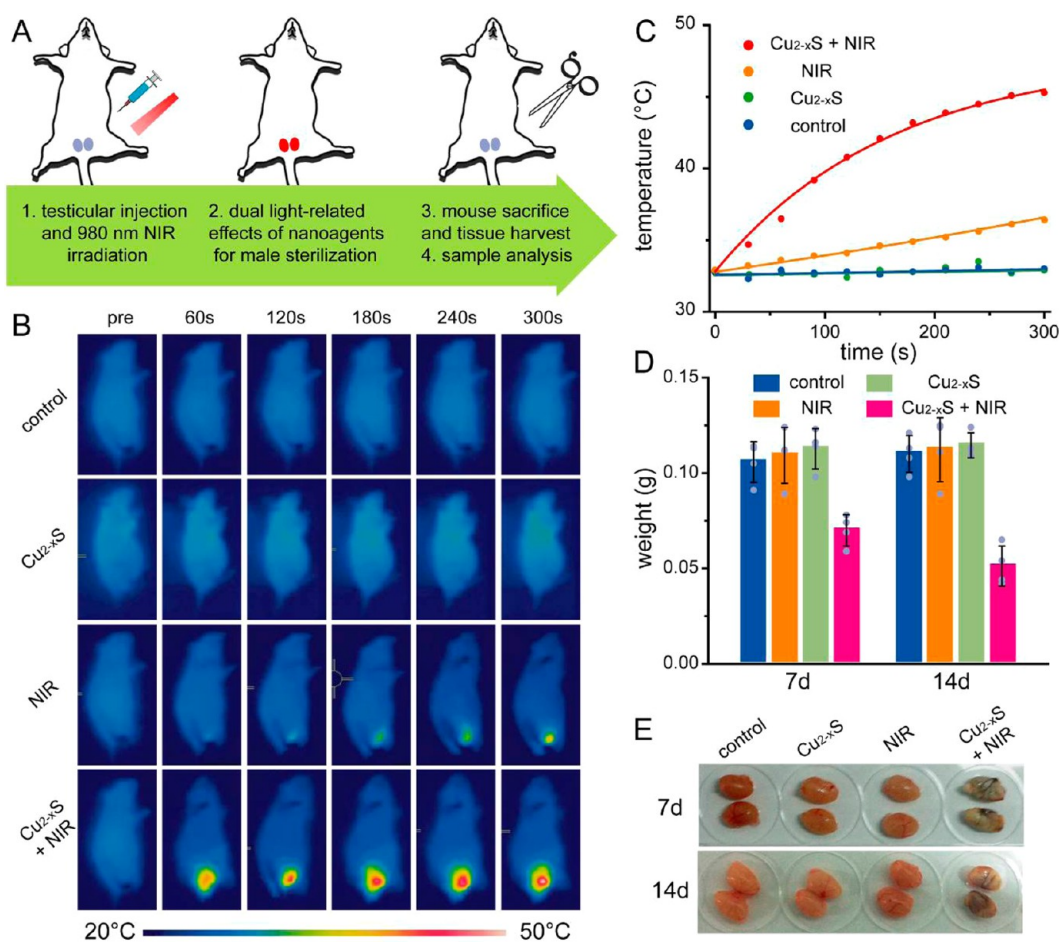
Figure 4. Schematic illustration of the experimental design of a mouse model (A). Thermal infrared images of mice (B) and changes of temperature as a function of irradiation time (C) under different treatments. Weights (D) and related photos (E) of mouse testicles before and after various treatments.

to significant apoptosis of cells due to the protein denaturation-triggered injury/death.[58,59] The results of total-protein electrophoresis demonstrated that the fewest proteins appeared on the gel in the $Cu_{2-x}S$+NIR group, which indicated that most cellular death occurred in this group (Figure 3F). As an important executive enzyme in the apoptosis signaling pathway, the expression of caspase 3 and its active form were used to confirm the degree of apoptosis.[60] The $Cu_{2-x}S$+NIR group had the most expression of caspase 3 as compared with the other three groups (Figure 3G). In addition, the active caspase-3 stripe in the $Cu_{2-x}S$+NIR group was much darker than those of other three groups, demonstrating the activation of caspase-3 and further serious cellular apoptosis. In accordance with these findings, $Cu_{2-x}S$ NCs could act as intelligent light-driven sterilants for permanent male sterilization *via* their synergic effects.

Figure 4A schematicly illustrates the *in vivo* protocol of light-induced male sterilization. First, healthy male mice were divided into four groups including control, $Cu_{2-x}S$, NIR, and $Cu_{2-x}S$+NIR. Second, temperature changes around the testicles in these groups were recorded *via* an infrared camera. As shown in

Figure 4B and C, the temperature still remained around 32 °C in the control and $Cu_{2-x}S$ groups, while the temperature continued to increase to 36 °C in the NIR group. More importantly, the temperature reached a value of 45 °C stage by stage in the $Cu_{2-x}S$+NIR group, which suggested that a controllable temperature around the testicles could be obtained by regulating the irradiation period and power intensity of the NIR laser. Furthermore, because of the facile ROS generation of nanocrystals upon NIR irradiation, we could reduce the light-induced hyperthermia and decrease incidental scrotal irritation in mice caused by high temperature. Third, the above mice were housed for several days and sacrificed at expected time points for further investigations. The testicles of these mice were separated, weighed, and analyzed *via* histological staining at each time point. Compared with the other groups, the weights of the testicles in the $Cu_{2-x}S$+NIR group decreased sharply after treatments (Figure 4D). Moreover, the testicles in the $Cu_{2-x}S$+NIR group thoroughly atrophied and shrunk in size 2 weeks after treatments (Figure 4E). These results demonstrated that high-performance dual light-driven effects of $Cu_{2-x}S$ NCs led to serious injury of the testicles, which
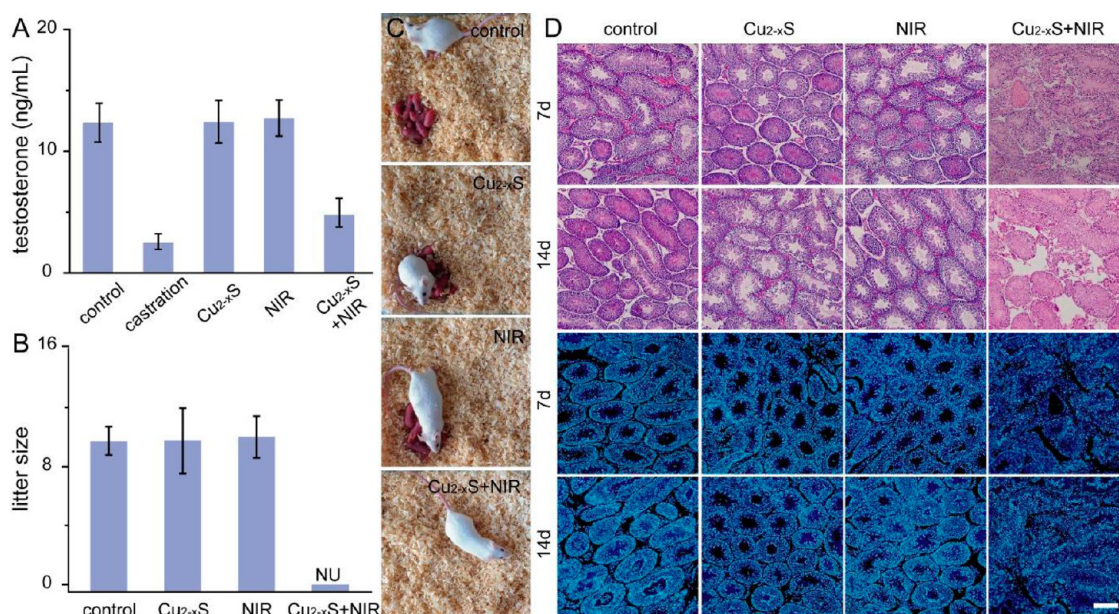
Figure 5. Levels of plasma testosterone (A), litter size (B), and related photos (C) after different treatments. NU indicates that there were no pups after the treatment with a 980 nm laser and $Cu_{2-x}S$ NCs. Histological images of mouse testicles stained by H&E and DAPI before and after various treatments (D). The scale bar equals 100 μm.

could be attributed to the protein denaturation in the testicles and apoptosis-associated pathway based on our total-protein electrophoresis and Western blotting analysis. Compared with a recent study, our approach could achieve permanent male sterilization under a relatively low temperature *via* the dual light-induced effect, whereas the photothermal effect caused by gold nanorods must include a higher hyperthermia treatment over 45 °C to gain total male infertility.[58] More importantly, these results demonstrated that ROS generated from $Cu_{2-x}S$ NCs upon NIR irradiation had an extreme photodynamic effect toward the destruction of testicles, which could act as a powerful assistant of nanocrystals' photothermal effect.

Malfunction of spermatogenesis caused by testicular damage could lead to the alteration of hormone levels. Testosterone, as the most important male hormone, could maintain sexuality and sexual functions.[61,62] Accordingly, testosterone levels in plasma of the above mice were determined *via* an enzyme-linked immunosorbent assay. Healthy male mice without any treatment were selected as control. The level of testosterone in the $Cu_{2-x}S$+NIR group decreased to a third of that of the control, which was still much higher than that in male mice after castration (Figure 5A). Our results suggested that the present technique for male sterilization could efficiently control the level of testosterone and support the retention of secondary sex characteristic. As is well known, a decrease of plasma testosterone usually lowers sexual functions and impairs reproduction functions.[63] We then investigated the potential effect on fertility of these male mice 2 weeks after various treatments. Male mice had lost their reproductive capacity partly or totally in the

$Cu_{2-x}S$+NIR group; thereby none of the female mice gave birth (Figure 5B and C). In contrast, female mice in other groups all gave birth with the same numbers of pups. To determine the changes in physiological structure of the testicles, histological inspections *via* H&E staining and DAPI staining were performed (Figure 5D). As expected, nearly all the Sertoli cells in the $Cu_{2-x}S$+NIR group were fragmented and degenerated as compared to other three groups. Moreover, enlarged images of H&E staining clearly indicated that $Cu_{2-x}S$ NCs could result in the total destruction of Sertoli cells *in vivo via* dual effects upon NIR irradiation (Figure S8). To provide more accurate results, we carried out a long-term investigation to determine whether the male sterilization was permanent. Two months after treatment, we could not harvest integrated testicles from the mice in the $Cu_{2-x}S$+NIR group owing to the serious atrophy in size. Taken together, both qualitative and quantitative results describe that the testicles from $Cu_{2-x}S$+NIR-treated mice were destroyed, which caused the functional disorder of spermatogenesis and further male infertility.

To determine whether $Cu_{2-x}S$ NCs led to any harmful effect or disease after systemic administration, a possible metabolic pathway and long-term toxicity were verified.[64−68] As shown in Figure 6A, $Cu_{2-x}S$ NCs mainly accumulated in the testicles, liver, and spleen after testicular injection. The amount of copper ions in the testicles decreased over time, but slightly increased in the spleen and liver. We ascribe the above phenomenon to the potential uptake−transport−release mechanism by macrophage-like cells in the testicles, indicating that our nanocrystals could be cleared by the reticuloendothelial system. Behavior observation and body weight
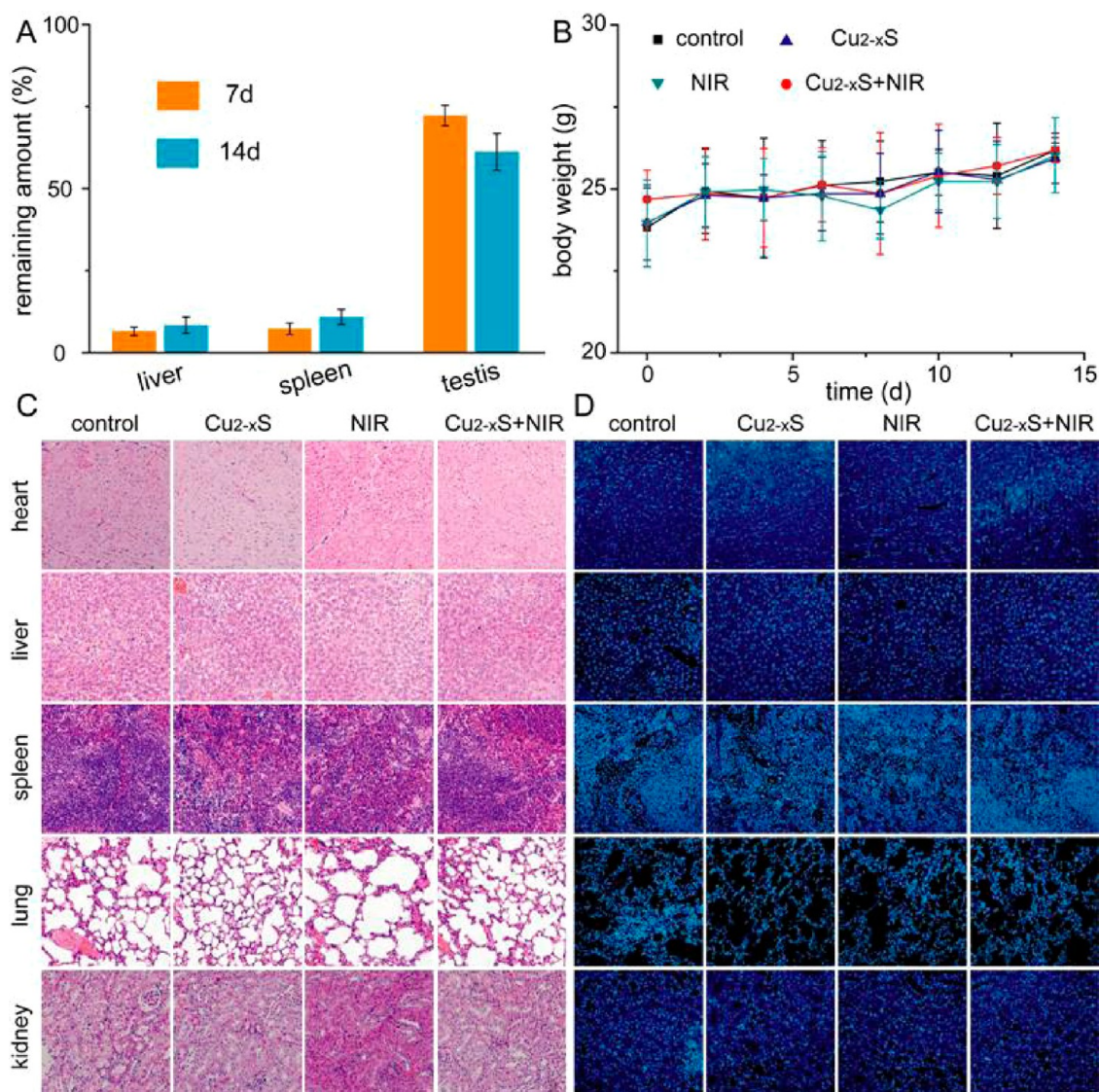
Figure 6. Time-dependent biodistribution of Cu$_{2-x}$S NCs after testicular injection (A). Changes in body weights (B), H&E-stained histological images of main organs (C), and DAPI-stained histological images of main organs (D). The scale bar equals 100 μm.

measurement further demonstrated that no remarkable differences occurred among all these groups (Figure 6B). In addition, no tissue damage associated with the testicular injection of Cu$_{2-x}$S NCs was found, and all organs presented a similar weight profile to those without any treatments (Figure 6C,D, Figure S9, and Table S2). To obtain quantitative assessments of toxicity, a blood biochemical assay and hematology analysis were carried out. All the parameters in the Cu$_{2-x}$S NCs-treated group were similar to those without any treatment and fell in the reference normal range (Figure S10). These results thereby indicate that Cu$_{2-x}$S NCs at the given dose did not cause *in vivo* toxicity effects and possess high biocompatibility.

CONCLUSION

In summary, a new platform for permanent male sterilization has been demonstrated *via* the photothermal

and photodynamic effects of plasmonic Cu$_{2-x}$S NCs upon NIR laser irradiation. To the best of our knowledge, this study was the first example showing that metal chalcogenides could act as smart light-driven sterilants in reproductive medicine. The potential mechanism of gonad injury could be ascribed to the protein denaturation and apoptosis-related death caused by the local hyperthermia and ROS generation of these nanocrystals under NIR excitation. Compared with surgical castration, chemical injections, and anti-fertility vaccines, our present procedure was a less invasive, more convenient, and more efficient one with ideal outcomes. Under a lower local temperature around the testicles, the combination of dual effects could result in a better sterilization efficacy rather than the photothermal effect alone, which extremely decreased unwanted heat-induced scrotal irritation. Furthermore, we investigated the plasma levels of testosterone,

litter size, long-term toxicity, and fate route after testicular injection. Accordingly, our present approach provided new insights for male sterilization *via* novel plasmonic nanomaterials and could be used to treat pet overpopulation and development of neutered experimental animals.

EXPERIMENTAL SECTION

Chemical and Materials. Oleylamine (OM), 1-octadecene (ODE), and calcein AM were obtained from Sigma-Aldrich. CuCl, sulfur powder, 6-amino caproic acid (6-ACA), and chloral hydrate were purchased from Aladdin Reagent. Trypsin, Dulbecco's modified Eagle's medium (DMEM), and fetal bovine serum were acquired from Sangon. Other reagents and solvents were procured from Beijing Chemicals. All chemical agents were of analytical grade and used directly without further purification. Water throughout all experiments was obtained *via* a Milli-Q water system.

Synthesis of Hydrophobic Cu$_{2-x}$S Nanocrystals. Cu$_{2-x}$S NCs were synthesized *via* a modified thermal decomposition method. Copper ion solution was prepared by dissolving CuCl (5 mmol) in OM (30 mL) at 100 °C under vacuum. Sulfur solution was prepared by dissolving sulfur power (2.5 mmol) in ODE (10 mL) at 180 °C under nitrogen until the color of the solution became transparent yellow. After mixing the above two solutions together at room temperature, the mixture was heated to 180 °C at a rate of 10 °C/min and kept at 180 °C for 15 min under nitrogen. The reaction was then quenched in a cold-bath to room temperature. After that, the product was precipitated by ethanol (60 mL) and redispersed in chloroform (20 mL) for further use.

Ligand Exchange Procedure. An aqueous solution (5 mL) containing 6-ACA (2 mmol) and NH$_3$·H$_2$O (2 mmol) was added into another solution containing hydrophobic Cu$_{2-x}$S NCs (0.1 g), ethanol (30 mL), water (10 mL), and hexane (35 mL). Under continuous magnetic stirring, this solution was heated to 70 °C and kept at this temperature for 6 h. Then, hydrophobic nanocrystals were transferred to the aqueous phase from the organic phase. Hydrophilic NCs were separated *via* centrifugation, collected after washing with water, and obtained *via* freeze-drying overnight.

Animal Administration. Kunming mice were purchased from Laboratory Animal Center of Jilin University (Changchun, China). All animal procedures were in accord with the guidelines of the Institutional Animal Care and Use Committee.

Cell Cultures. Sertoli cells were harvested from 2-week-old Kunming mice. Mice were euthanized and immersed in an ethanol solution (75%) for several minutes. Testicles were separated and cut into pieces after the removal of tunica albuginea and blood vessels. Trypsin containing collagenase IV and EDTA was applied for the preparation of the cell suspension. Obtained Sertoli cells were cultured in DMEM with fetal bovine serum (10%), penicillin (100 U/mL), and streptomycin (100 U/mL) in a humidified incubator (37 °C, 5% CO$_2$). To obtain purified cells, a hypotonic solution was used by discarding the other cell suspension owing to the intrinsic adherent property of Sertoli cells.

Cytotoxicity Studies. Sertoli cells were cultured in a 96-well plate with a density of 5 × 10^3 per well for 12 h. Solutions containing Cu$_{2-x}$S NCs were added to the culture medium. After incubation for 24 h, the residual nanocrystals in the medium were removed. Cells were treated with MTT for another 4 h, which was followed by the addition of DMSO to dissolve the formazan crystals. A Bio-Rad model-680 microplate reader was used to measure the absorbance at a wavelength of 570 nm. The absorbance of Cu$_{2-x}$S NCs at different concentrations was measured as the deductible background. Six replicates were done for each group, and the viability was normalized to the viability in the absence of Cu$_{2-x}$S NCs.

Cellular Viability Observation. Sertoli cells with a density of 1 × 10^4 were plated in a six-well plate for 12 h. After the cells were washed twice by 0.9% NaCl solution, Cu$_{2-x}$S NCs were added to the cell culture medium. After incubation for 24 h, cells were washed with 0.9% NaCl solution to remove the remaining nanocrystals. Then, Sertoli cells were stained with propidium iodide (PI) and calcein AM. Fluorescence images were collected on an Olympus BX-51 optical system.

Light-Induced Cytotoxicity. Sertoli cells were cultured in a 96-well plate at a density of 5 × 10^3 per well for 12 h. Solutions containing Cu$_{2-x}$S NCs were added to the culture medium. After 4 h of incubation, Sertoli cells were irradiated by a 980 nm laser with a power intensity of 1 W/cm^2 for different periods. Then, the cells were incubated for another 24 h, and the cell viability was evaluated *via* MTT assay.

Live/Dead Staining. Sertoli cells in a six-well plate were incubated with Cu$_{2-x}$S NCs (100 μg/mL) for 4 h, irradiated with a 980 nm laser (1 W/cm^2, 5 min), and stained with calcein AM and PI. Fluorescence microscopy images were collected *via* an Olympus BX-51 optical system. A 0.4% trypan blue solution was applied to distinguish live/dead cells under an optical microscope.

Fluorescence Imaging of ROS Generation. Solutions containing H$_2$O$_2$ and NaClO with different concentrations were first mixed with DCFH-DA. Other samples in our design were treated with Cu$_{2-x}$S NCs and NIR laser irradiation as expected, as well as mixed with DCFH-DA. Then, fluorescence imaging of the above samples after various treatments was carried out on a Kodak *In-vivo* Imaging System (Fx Pro) with an excitation wavelength of 490 nm.

ROS Detection. Sertoli cells with a density of 1 × 10^4 were plated in six-well plates for 12 h. Cells were incubated with Cu$_{2-x}$S NCs (100 μg/mL) for 4 h and irradiated with a 980 nm laser (1 W/cm^2, 5 min). The above cell medium was replaced with DCFH-DA solution, followed by incubation for another 30 min at 37 °C in the dark. The group without any treatment was noted as the control. Fluorescence microscopy images were collected on an Olympus BX-51 optical system. For the quantitative results, Sertoli cells were trypsinized and subjected to flow cytometry analysis. All cells were irradiated to prepare samples for flow cytometry.

Contributions of Photothermal Effect and Photodynamic Effect. Sertoli cells with a density of 1 × 10^4 were plated in six-well plates for 12 h. Cells were first incubated with Cu$_{2-x}$S NCs (100 μg/mL) for 4 h, treated with UA (0.25 mM) and DMSO (0.5%) for 30 min, and irradiated with a 980 nm laser (1 W/cm^2, 5 min). The inhibition of ROS generation was determined on an Olympus BX-51 optical system. For the MTT assay, cells (5 × 10^3 per well) were cultured in a 96-well plate for 12 h. Solutions containing Cu$_{2-x}$S NCs were added to the above culture medium. After 4 h of incubation, cells were treated with UA and DMSO for 30 min and irradiated by a 980 nm laser (1 W/cm^2, 6 min). Twenty-four hours later, cell viability was evaluated *via* an MTT assay.

Total-Protein Electrophoresis. Sertoli cells were incubated with Cu$_{2-x}$S NCs (100 μg/mL) for 4 h and irradiated with a 980 nm laser (1 W/cm^2, 5 min). To test the amount of total protein, cells after various treatments and 12 h of incubation were lyzed and subjected to electrophoresis. Lysates were resolved by SDS-PAGE. Gel was stained *via* Coomassie Brilliant Blue, decolorized, and scanned.

Apoptosis/Necrosis Analysis. Sertoli cells were incubated with Cu$_{2-x}$S NCs (100 μg/mL) for 4 h and irradiated with a 980 nm laser (1 W/cm^2, 5 min). All cells should receive equal irradiation in our system. Without further incubation, an annexin V-FITC apoptosis detection kit was used to detect the percentage of apoptosis and necrosis. Intact cells (FITC−/PI−), early apoptotic cells (FITC+/PI−), late apoptotic/necrotic cells (FITC+/PI+), and damaged cells (FITC−/PI+) were quantified by fluorescence-activated cell sorting flow cytometry.

Caspase-3/Active Caspase-3 Expression. Sertoli cells were incubated with Cu$_{2-x}$S NCs (100 μg/mL) for 4 h and irradiated with a 980 nm laser (1 W/cm^2, 5 min). The protein sample obtained from the above cells without incubation was separated by

SDS-PAGE, transferred onto a polyvinylidene difluoride (PVDF) membrane, and analyzed *via* immunoblotting using a chemiluminescence system (Santa Cruz, CA, USA). Protein levels were normalized to β-actin. The primary antibodies were rabbit anti-β-actin, rabbit anticaspase-3, and rabbit anti-active caspase-3. Horseradish peroxidase (HRP)-conjugated anti-rabbit IgG was selected as the secondary antibody to amplify the signals.

Thermal Imaging. Male mice were divided into four groups including control, $Cu_{2-x}S$, NIR, and $Cu_{2-x}S$+NIR. Mice were anesthetized *via* intraperitoneal injection of chloral hydrate (10%). Solutions containing $Cu_{2-x}S$ NCs (2 mg/mL, 100 μL) were administrated by testicular injections in $Cu_{2-x}S$ and $Cu_{2-x}S$+NIR groups. To obtain thermal imaging, mice in the NIR and $Cu_{2-x}S$+NIR groups were irradiated by a 980 nm laser with a power density of 1 W/cm^2 for 5 min. The spot size of the laser beam was adjusted to cover the total region of the testicles. All the groups were imaged *via* an IR thermal camera (FLIR I3). Meanwhile, changes of testicle temperatures were recorded.

Testicle Harvest and Analysis. Mice were sacrificed at expected time points after treatments ($n = 4$). Testicles were harvested, weighed, and subjected to histology analysis.

Hormone Assay and Fertility Evaluation. Blood of male mice in the above groups was collected 2 weeks after treatments ($n = 4$). Plasma testosterone levels were measured *via* a double antibody sandwich ELISA assay. Two weeks after treatments, mice from the above groups were submitted to the mating tests ($n = 4$). A male mouse was caged with two female mice for 10 days. To determine the numbers of pups in all groups, female mice were separated from the male mice after mating.

Biodistribution Study. $Cu_{2-x}S$ NCs (2 mg/mL, 100 μL) were administrated by testicular injection ($n = 4$). Mice were sacrificed at expected time points. Main organs including testicles, spleens, and livers were harvested, lyzed, and subjected to ICP-MS analysis.

Body Weight Measurement. Male mice from the above groups were weighed after treatments ($n = 4$). The body weights of the above mice were recorded for 2 weeks.

Histology Analysis. Mice from the above groups were sacrificed 2 weeks after treatments. Main organs were harvested and fixed in buffered formalin (10%). The organs were embedded in paraffin, sectioned, and stained with hematoxylin and eosin (H&E). Moreover, fluorescence images of DAPI-stained organs were collected on an Olympus BX-51 optical system.

Hematology Analysis and Blood Biochemical Assay. Blood of mice in the $Cu_{2-x}S$+NIR group and control group was collected ($n = 4$). Main indicators for kidney and liver were investigated *via* a clinical route.

Statistical Analysis. All data were expressed in the present article as mean result $\pm$ standard deviation (SD). The statistical analysis was performed *via* Origin 8.0 software.

Conflict of Interest: The authors declare no competing financial interest.

Supporting Information Available: The Supporting Information is available free of charge on the ACS Publications website at DOI: 10.1021/acsnano.5b04380.

Additional figures and tables as described in the text (PDF)

REFERENCES AND NOTES

1. Bowen, R. Male Contraceptive Technology for Nonhuman Male Mammals. *Anim. Reprod. Sci.* **2008**, *105*, 139–143.
2. Gray, M.; Cameron, E. Does Contraceptive Treatment in Wildlife Result in Side Effects? A Review of Quantitative and Anecdotal Evidence. *Reproduction* **2010**, *139*, 45–55.
3. Kutzler, M.; Wood, A. Non-surgical Methods of Contraception and Sterilization. *Theriogenology* **2006**, *66*, 514–525.
4. Howe, L. Surgical Methods of Contraception and Sterilization. *Theriogenology* **2006**, *66*, 500–509.
5. Kustritz, M. Effects of Surgical Sterilization on Canine and Feline Health and on Society. *Reprod. Dom. Anim.* **2012**, *47*, 214–222.
6. Munks, M. Progress in Development of Immunocontraceptive Vaccines for Permanent Non-surgical Sterilization of Cats and Dogs. *Reprod. Dom. Anim.* **2012**, *47*, 223–227.
7. Cooper, D.; Larsen, E. Immunocontraception of Mammalian Wildlife: Ecological and Immunogenetic Issues. *Reproduction* **2006**, *132*, 821–828.
8. Kim, J.; Piao, Y.; Hyeon, T. Multifunctional Nanostructured Materials for Multimodal Imaging, and Simultaneous Imaging and Therapy. *Chem. Soc. Rev.* **2009**, *38*, 372–390.
9. Sailor, M.; Park, J. Hybrid Nanoparticles for Detection and Treatment of Cancer. *Adv. Mater.* **2012**, *24*, 3779–3802.
10. Cai, W.; Chen, X. Nanoplatforms for Targeted Molecular Imaging in Living Subjects. *Small* **2007**, *3*, 1840–1854.
11. Cheng, L.; Wang, C.; Feng, L.; Yang, K.; Liu, Z. Functional Nanomaterials for Phototherapies of Cancer. *Chem. Rev.* **2014**, *114*, 10869–10939.
12. Xu, L.; Cheng, L.; Wang, C.; Peng, R.; Liu, Z. Conjugated Polymers for Photothermal Therapy of Cancer. *Polym. Chem.* **2014**, *5*, 1573–1580.
13. Zhang, Z.; Wang, J.; Chen, C. Gold Nanorods Based Platforms for Light-Mediated Theranostics. *Theranostics* **2013**, *3*, 223–238.
14. Lal, S.; Clare, S.; Halas, N. Nanoshell-Enhanced Photothermal Cancer Therapy: Impending Clinical Impact. *Acc. Chem. Res.* **2008**, *41*, 1842–1851.
15. Liu, Z.; Liu, J.; Wang, R.; Du, Y.; Ren, J.; Qu, X. An Efficient Nano-Based Theranostic System for Multi-Modal Imaging-Guided Photothermal Sterilization in Gastrointestinal Tract. *Biomaterials* **2015**, *56*, 206–218.
16. Cai, X.; Zhang, Y.; Xia, Y.; Wang, L. Photoacoustic Microscopy in Tissue Engineering. *Mater. Today* **2013**, *16*, 67–77.
17. Xia, Y.; Li, W.; Cobley, C.; Chen, J.; Xia, X.; Zhang, Q.; Yang, M.; Cho, E.; Brown, P. Gold Nanocages: From Synthesis to Theranostic Applications. *Acc. Chem. Res.* **2011**, *44*, 914–924.
18. Halas, N. The Photonic Nanomedicine Revolution: Let the Human Side of Nanotechnology Emerge. *Nanomedicine* **2009**, *4*, 369–371.
19. Yang, K.; Xu, H.; Cheng, L.; Sun, C.; Wang, J.; Liu, Z. *In Vitro* and *in Vivo* Near-Infrared Photothermal Therapy of Cancer Using Polypyrrole Organic Nanoparticles. *Adv. Mater.* **2012**, *24*, 5586–5592.
20. Zhang, Z.; Wang, J.; Nie, X.; Wen, T.; Ji, Y.; Wu, X.; Zhao, Y.; Chen, C. Near Infrared Laser-Induced Targeted Cancer Therapy Using Thermoresponsive Polymer Encapsulated Gold Nanorods. *J. Am. Chem. Soc.* **2014**, *136*, 7317–7326.
21. Chen, M.; Tang, S.; Guo, Z.; Wang, X.; Mo, S.; Huang, X.; Liu, G.; Zheng, N. Core-Shell Pd@Au nanoplates as Theranostic Agents for *in-Vivo* Photoacoustic Imaging, CT Imaging, and Photothermal Therapy. *Adv. Mater.* **2014**, *26*, 8210–8216.
22. Zha, Z.; Yue, X.; Ren, Q.; Dai, Z. Uniform Polypyrrole Nanoparticles with High Photothermal Conversion Efficiency for Photothermal Ablation of Cancer Cells. *Adv. Mater.* **2013**, *25*, 777–782.
23. Liu, Y.; Zhao, Y.; Sun, B.; Chen, C. Understanding the Toxicity of Carbon Nanotubes. *Acc. Chem. Res.* **2013**, *46*, 702–713.
24. Yang, K.; Gong, H.; Shi, X.; Wan, J.; Zhang, Y.; Liu, Z. *In Vivo* Biodistribution and Toxicology of Functionalized Nano-Graphene Oxide in Mice after Oral and Intraperitoneal Administration. *Biomaterials* **2013**, *34*, 2787–2795.
25. Huang, X.; Zhang, F.; Sun, X.; Choi, K.; Niu, G.; Zhang, G.; Guo, J.; Lee, S.; Chen, X. The Genotype-Dependent Influence of Functionalized Multiwalled Carbon Nanotubes on Fetal Development. *Biomaterials* **2014**, *35*, 856–865.
26. Goel, S.; Chen, F.; Cai, W. Synthesis and Biomedical Applications of Copper Sulfide Nanoparticles: From Sensors to Theranostics. *Small* **2014**, *10*, 631–645.
27. Chen, F.; Hong, H.; Goel, S.; Graves, S.; Orbay, H.; Ehlerding, E.; Shi, S.; Theuer, C.; Nickles, R.; Cai, W. *In Vivo* Tumor Vasculature Targeting of CuS@MSN based Theranostic Nanomedicine. *ACS Nano* **2015**, *9*, 3926–3934.

28. Zhou, M.; Zhang, R.; Huang, M.; Lu, W.; Song, S.; Melancon, M.; Tian, M.; Liang, D.; Li, C. A Chelator-Free Multifunctional [^{64}Cu]CuS Nanoparticle Platform for Simultaneous Micro-PET/CT Imaging and Photothermal Ablation Therapy. *J. Am. Chem. Soc.* **2010**, *132*, 15351–15358.

29. Ku, G.; Zhou, M.; Song, S.; Huang, Q.; Hazle, J.; Li, C. Copper Sulfide Nanoparticles as a New Class of Photoacoustic Contrast Agent for Deep Tissue Imaging at 1064 nm. *ACS Nano* **2012**, *6*, 7489–7496.

30. Tian, Q.; Tang, M.; Sun, Y.; Zou, R.; Chen, Z.; Zhu, M.; Yang, S.; Wang, J.; Wang, J.; Hu, J. Hydrophilic Flower-Like CuS Superstructures as an Efficient 980 nm Laser-Driven Photothermal Agents for Ablation of Cancer Cells. *Adv. Mater.* **2011**, *23*, 3542–3547.

31. Bai, J.; Liu, Y.; Jiang, X. Multifunctional PEG-GO/CuS Nanocomposites for Near-Infrared Chemo-Photothermal Therapy. *Biomaterials* **2014**, *35*, 5805–5813.

32. Dong, K.; Liu, Z.; Li, Z.; Ren, J.; Qu, X. Hydrophobic Anticancer Drug Delivery by a 980 nm Laser-Driven Photothermal Vehicle for Efficient Synergistic Therapy of Cancer Cells in Vivo. *Adv. Mater.* **2013**, *25*, 4452–4458.

33. Mou, J.; Liu, C.; Li, P.; Chen, Y.; Xu, H.; Wei, C.; Song, L.; Shi, J.; Chen, H. A Facile Synthesis of Versatile Cu$_{2-x}$S Nanoprobe for Enhanced MRI and Infrared Thermal/Photoacoustic Multimodal Imaging. *Biomaterials* **2015**, *57*, 12–21.

34. Luther, J.; Jain, P.; Ewers, T.; Alivisatos, A. Localized Surface Plasmon Resonances Arising from Free Carriers in Doped Quantum Dots. *Nat. Mater.* **2011**, *10*, 361–366.

35. Scotognella, F.; Della Valle, G.; Kandada, A.; Dorfs, D.; Zavelani-Rossi, M.; Conforti, M.; Miszta, K.; Comin, A.; Korobchevskaya, K.; Lanzani, G.; Manna, L.; Tassone, F. Plasmon Dynamics in Colloidal Cu$_{2-x}$Se Nanocrystals. *Nano Lett.* **2011**, *11*, 4711–4717.

36. Hessel, C.; Pattani, V.; Rasch, M.; Panthani, M.; Koo, B.; Tunnell, J.; Korgel, B. Copper Selenide Nanocrystals for Photothermal Therapy. *Nano Lett.* **2011**, *11*, 2560–2566.

37. Ding, X.; Liow, C.; Zhang, M.; Huang, R.; Li, C.; Shen, H.; Liu, M.; Zou, Y.; Gao, N.; Zhang, Z.; Li, Y.; Wang, Q.; Li, S.; Jiang, J. Surface Plasmon Resonace Enhanced Light Absorption and Photothermal Therapy in the Second Near-Infrared Window. *J. Am. Chem. Soc.* **2014**, *136*, 15684–15693.

38. Li, W.; Zamani, R.; Gil, P.; Pelaz, B.; Ibáñez, M.; Cadavid, D.; Shavel, A.; Alvarez-Puebla, R.; Parak, W.; Arbiol, J.; Cabot, A. CuTe Nanocrystals: Shape and Size Control, Plasmonic Properties, and Use as SERS Probes and Photothermal Agents. *J. Am. Chem. Soc.* **2013**, *135*, 7098–7101.

39. Kriegel, I.; Jiang, C.; Rodríguez-Fernández, J.; Schaller, R.; Talapin, D.; da Como, E.; Feldmann, J. Tuning the Excitonic and Plasmonic Properties of Copper Chalcogenide Nanocrystals. *J. Am. Chem. Soc.* **2012**, *134*, 1583–1590.

40. Zhao, Y.; Pan, H.; Lou, Y.; Qiu, X.; Zhu, J.; Burda, C. Plasmonic Cu$_{2-x}$S Nanocrystals: Optical and Structural Properties of Copper-Deficient Copper (I) Sulfides. *J. Am. Chem. Soc.* **2009**, *131*, 4253–4261.

41. Dorfs, D.; Härtling, T.; Miszta, K.; Bigall, N.; Kim, M.; Genovese, A.; Falqui, A.; Povia, M.; Manna, L. Reversible Tunability of the Near-Infrared Valence Band Plasmon Resonance in Cu$_{2-x}$Se Nanocrystals. *J. Am. Chem. Soc.* **2011**, *133*, 11175–11180.

42. Xie, Y.; Riedinger, A.; Prato, M.; Casu, A.; Genovese, A.; Guardia, P.; Sottini, S.; Sangregorio, C.; Miszta, K.; Ghosh, S.; Pellegrino, T.; Manna, L. Copper Sulfide Nanocrystals with Tunable Composition by Reduction of Covellite Nanocrystals with Cu$^+$ Ions. *J. Am. Chem. Soc.* **2013**, *135*, 17630–17637.

43. Lesnyak, V.; Brescia, R.; Messina, G.; Manna, L. Cu Vacancies Boost Cation Exchange Reactions in Copper Selenide Nanocrystals. *J. Am. Chem. Soc.* **2015**, *137*, 9315–9323.

44. Xie, Y.; Carbone, L.; Nobile, C.; Grillo, V.; D'Agostino, S.; Della Sala, F.; Giannini, C.; Altamura, D.; Oelsner, C.; Kryschi, C.; Cozzoli, P. Metallic-like Stoichiometric Copper Sulfide Nanocrystals: Phase- and Shape Selective Synthesis, Near-Infrared Surface Plasmon Resonance Properties, and Their Modeling. *ACS Nano* **2013**, *7*, 7352–7369.

45. Kadiiska, M.; Hanna, P.; Hernandez, L.; Mason, R. In Vivo Evidence of Hydroxyl Radical Formation after Acute Copper and Ascorbic Acid Intake: Electron Spin Resonance Spin-Trapping Investigation. *Mol. Pharmacol.* **1992**, *42*, 723–729.

46. Kadiiska, M.; Mason, R. In Vivo Copper-Mediated Free Radical Production: an ESR Spin-Trapping Study. *Spectrochim. Acta, Part A* **2002**, *58*, 1227–1239.

47. Wang, S.; Riedinger, A.; Li, H.; Fu, C.; Liu, H.; Li, L.; Liu, T.; Tan, L.; Barthel, M.; Pugliese, G.; De Donato, F.; D'Abbusco, M.; Meng, X.; Manna, L.; Meng, H.; Pellegrino, T. Plasmonic Copper Sulfide Nanocrystals Exhibiting Near-Infrared Photothermal and Photodynamic Therapeutic Effects. *ACS Nano* **2015**, *9*, 1788–1800.

48. Poulose, A.; Veeranarayanan, S.; Mohamed, S.; Nagaoka, Y.; Aburto, R.; Mitcham, T.; Ajayan, P.; Bouchard, R.; Sakamoto, Y.; Yoshida, Y.; Maekawa, T.; Kumar, D. Multi-Stimuli Responsive Cu$_2$S Nanocrystals as Trimodal Imaging and Synergistic Chemo-Photothermal Therapy Agents. *Nanoscale* **2015**, *7*, 8378–8388.

49. Tian, Q.; Jiang, F.; Zou, R.; Liu, Q.; Chen, Z.; Zhu, M.; Yang, S.; Wang, J.; Wang, J.; Hu, J. Hydrophilic Cu$_9$S$_5$ Nanocrystals: A Photothermal Agent with a 25.7% Heat Conversion Efficiency for Photothermal Ablation of Cancer Cells in Vivo. *ACS Nano* **2011**, *5*, 9761–9771.

50. Liu, Y.; Ai, K.; Liu, J.; Deng, M.; He, Y.; Lu, L. Dopamine-Melanin Colloidal Nanospheres: An Efficient Near-Infrared Photothermal Therapeutic Agent for in Vivo Cancer Therapy. *Adv. Mater.* **2013**, *25*, 1353–1359.

51. Lovell, J.; Jin, C.; Huynh, E.; Jin, R.; Kim, C.; Rubinstein, J.; Chan, W.; Cao, W.; Wang, L.; Zheng, G. Porphysome Nanovesicles Generated by Porphyrin Bilayers for Use as Multimodal Biophotonic Contrast Agents. *Nat. Mater.* **2011**, *10*, 324–332.

52. Wang, L.; Sun, Q.; Wang, X.; Wen, T.; Yin, J.; Wang, P.; Bai, R.; Zhang, X.; Zhang, L.; Lu, A.; Chen, C. Using Hollow Carbon Nanospheres as a Light-Induced Free Radical Generator to Overcome Chemotherapy Resistance. *J. Am. Chem. Soc.* **2015**, *137*, 1947–1955.

53. Pan, L.; Liu, J.; Shi, J. Intranuclear Photosensitizer Delivery and Photosensitization for Enhanced Photodynamic Therapy with Ultralow Irradiance. *Adv. Funct. Mater.* **2014**, *24*, 7318–7327.

54. Lin, Y.; Haynes, C. Impacts of Mesoporous Silica Nanoparticle Size, Pore Ordering, and Pore Integrity on Hemolytic Activity. *J. Am. Chem. Soc.* **2010**, *132*, 4834–4842.

55. Liu, Z.; Dong, K.; Liu, J.; Han, X.; Ren, J.; Qu, X. Anti-Biofouling Polymer-Decorated Lutetium-Based Nanoparticulate Contrast Agents for in Vivo High-Resolution Trimodal Imaging. *Small* **2014**, *10*, 2429–2438.

56. Ju, E.; Liu, Z.; Du, Y.; Tao, Y.; Ren, J.; Qu, X. Heterogeneous Assembled Nanocomplexes for Ratiometric Detection of Highly Reactive Oxygen Species in Vitro and in Vivo. *ACS Nano* **2014**, *8*, 6014–6023.

57. Chen, T.; Hu, Y.; Cen, Y.; Chu, X.; Lu, Y. A Dual-Emission Fluorescent Nanocomplex of Gold-Cluster-Decorated Silica Particles for Live Cell Imaging of Highly Reactive Oxygen Species. *J. Am. Chem. Soc.* **2013**, *135*, 11595–11602.

58. Li, W.; Sun, C.; Wang, F.; Wang, Y.; Zhai, Y.; Liang, M.; Liu, W.; Liu, Z.; Wang, J.; Sun, F. Achieving a New Controllable Male Contraception by the Photothermal Effect of Gold Nanorods. *Nano Lett.* **2013**, *13*, 2477–2484.

59. Cabiscol, E.; Tamarit, J.; Ros, J. Oxidative Stress in Bacteria and Protein Damage by Reactive Oxygen Species. *Int. Microbiol.* **2000**, *3*, 3–8.

60. Porter, A.; Jänicke, R. Emerging roles of caspase-3 in apoptosis. *Cell Death Differ.* **1999**, *6*, 99–104.

61. Vanderstichel, R.; Forzán, N.; Pérez, G.; Serpell, J.; Garde, E. Changes in Blood Testosterone Concentrations after Surgical and Chemical Sterilization of Male Free-Roaming Dogs in Southern Chile. *Theriogenology* **2015**, *83*, 1021–1027.

62. Kelly, D.; Jones, T. Testosterone: A Vascular Hormone in Health and Disease. *J. Endocrinol.* **2013**, *217*, R47–R71.

63. Anderson, R.; Baird, D. Male Contraception. *Endocr. Rev.* **2002**, *23*, 735–762.

64. Cheng, L.; Yang, K.; Shao, M.; Lu, X.; Liu, Z. *In Vivo* Pharmacokinetics, Long-Term Biodistribution and Toxicology Study of Functionalized Upconversion Nanoparticles in Mice. *Nanomedicine* **2011**, *6*, 1327–1340.

65. Liu, Z.; Pu, F.; Huang, S.; Yuan, Q.; Ren, J.; Qu, X. Long-Circulating Gd_2O_3:Yb^{3+},Er^{3+} Upconversion Nanoprobes as High-Performance Contrast Agents for Multi-Modality Imaging. *Biomaterials* **2013**, *34*, 1712–1721.

66. Liu, Z.; Pu, F.; Liu, J.; Jiang, L.; Yuan, Q.; Li, Z.; Ren, J.; Qu, X. PEGylated Hybrid Ytterbia Nanoparticles as High-Performance Diagnostic Probes for *in Vivo* Magnetic Resonance and X-Ray Computed Tomography Imaging with Low Systemic Toxicity. *Nanoscale* **2013**, *5*, 4252–4261.

67. Liu, Z.; Ju, E.; Liu, J.; Du, Y.; li, Z.; Yuan, Q.; Ren, J.; Qu, X. Direct Visualization of Gastrointestinal Tract with Lanthanide-Doped $BaYbF_5$ Upconversion Nanoprobes. *Biomaterials* **2013**, *34*, 7444–7452.

68. Xiong, L.; Yang, T.; Yang, Y.; Xu, C.; Li, F. Long-Term *in Vivo* Biodistribution Imaging and Toxicity of Polyacrylic Acid-Coated Upconversion Nanophosphors. *Biomaterials* **2010**, *31*, 7078–7085.

ARTICLE